applied sciences

MDPI

*Article*

# Stress Evolution and Rock Burst Prevention in Triangle Coal Pillars under the Influence of Penetrating Faults: A Case Study

**Wenhao Guo [1], Xuezhou Ma [1,*], Yingyuan Wen [1,2] and Xiaojie Cao [1]**

[1] School of Geology and Mining Engineering, Xinjiang University, Urumqi 830000, China; ilikemassa@163.com (W.G.)
[2] School of Mines, China University of Mining and Technology, Xuzhou 221116, China
* Correspondence: maxuezhou0209@163.com

**Abstract:** The occurrence of rock bursts due to penetrating faults are frequent in China, thereby limiting the safe production of coal mines. Based on the engineering background of a 501 working face in a TB coal mine, this paper investigates stress and energy evolution during the excavation of this working face due to multiple penetrating faults. Utilizing both theoretical analysis and numerical simulations, this study reveals the rock burst mechanism within the triangular coal pillar influenced by the penetrating faults. Based on the evolution of stress within the triangular coal pillar, a stress index has been devised to categorize both the rock burst danger regions and the levels of rock burst risks associated with the triangular coal pillar. Furthermore, targeted stress relief measures are proposed for various energy accumulation areas within the triangular coal pillar. The results demonstrate that: (1) the superimposed tectonic stress resulting from the T6 and T5 penetrating faults exhibits asymmetric distribution and has an influence range of about 90 m in the triangular coal pillar, reaching a peak value of 11.21 MPa at a distance of 13 m from the fault plane; (2) affected by the barrier effect of penetrating faults, the abutment stress of the working face is concentrated in the triangular coal pillar, and the magnitude of the abutment stress is positively and negatively correlated with the fault plane barrier effect and the width of the triangular coal pillar, respectively; (3) the exponential increase in abutment stress and tectonic stress as the width of the triangular coal pillar decreases leads to a high concentration of static stress, which induces pillar burst under the disturbance of dynamic stress from fault activation; (4) the numerical simulation shows that when the working face is 150 m away from the fault, the static stress and accumulated energy in the triangle coal pillar begins to rise, reaching the peak at 50 m away from the fault, which is consistent with the theoretical analysis; (5) the constructed stress index indicates that the triangular coal pillar exhibits moderate rock burst risks when its width is between 73 to 200 m, and exhibits high rock burst risks when the width is within 0 to 73 m. The energy accumulation pattern of the triangular coal pillar reveals that separate stress relief measures should be implemented within the ranges of 50 to 150 m and 0 to 50 m, respectively, in order to enhance the effectiveness of stress relief. Blasting stress relief measures for the roof and coal are proposed, and the effectiveness of these measures is subsequently verified.

**Keywords:** triangle coal pillar; penetrating fault; stress evolution; rock burst

check for updates

**Citation:** Guo, W.; Ma, X.; Wen, Y.; Cao, X. Stress Evolution and Rock Burst Prevention in Triangle Coal Pillars under the Influence of Penetrating Faults: A Case Study. *Appl. Sci.* **2024**, *14*, 8585. https://doi.org/10.3390/app14198585

Academic Editor: Tiago Miranda

Received: 6 August 2024
Revised: 14 September 2024
Accepted: 19 September 2024
Published: 24 September 2024

**Copyright:** © 2024 by the authors. Licensee MDPI, Basel, Switzerland. This article is an open access article distributed under the terms and conditions of the Creative Commons Attribution (CC BY) license (https://creativecommons.org/licenses/by/4.0/).

## 1. Introduction

Influenced by the tectonic evolution of the Tianshan Mountains [1,2], many faults exist in the TB mine in the Liuhuanggou mining area, which is located at the foot of the Tianshan Mountains. The 501 working face studied in this paper exposed 28 faults during mining, including 5 penetrating faults, which caused frequent high-energy microseismic events when the working face was excavated. Triangle coal pillar is formed between the working face and the penetrating fault when the fault tends to penetrate the working face [3]. The triangular coal pillar is affected by the superposition of tectonic stress [4] and abutment

stress [5] during the mining process of the working face. Its stress evolution is complex and the concentration is high, which induces dynamic disasters such as pillar burst [3,6], and seriously restricts the safe production of the coal mine. For example, on 3 November 2011, when the 21,221 working face of the Qianqiu Coal Mine was excavated for the large F16 fault, rock burst occurred in the triangular coal pillar and caused 10 deaths [7]. On 1 April 2012, a rock burst occurred during the mining of the triangular coal pillar formed by f3110-1 and f3109-1 faults in the Chaoyang Coal Mine, resulting in 17 injuries or deaths [8].

Some scholars have conducted a thorough investigation into the mechanisms through which tectonic stress and fault activation trigger rock bursts during excavation of the working face towards the fault. Yang et al. [9] and Zhu et al. [10] revealed that fault tectonic stress is an important factor in rock burst through stress monitoring data and numerical simulation; they found that the proximity of the fault correlates positively with tectonic stress. Wang et al. [11] and Li et al. [12] investigated the influence of the roof structure on fault activation by establishing mechanical models for the fault and the roof. Xiao et al. [13] revealed that the excavation of the working face towards the fault induced the activation of the fault, releasing high-energy microseisms, which induced coal pillar burst with high static stress. Zhang et al. [14] demonstrated through numerical simulations that the maximum principal stress difference between the two sides of the fault is the main reason for fault shear-slip. Jiang et al.'s [15] analysis of the microseismic data reveals that fault activation occurs approximately 250–350 m ahead of the working face. By establishing numerical models, Cao et al. [16] and Kong et al. [17] found that dynamic stress from fault activation increases the rock burst hazard for the coal pillar. Furthermore, the energy and distance of fault microseisms are positively and negatively related to the stability of the coal seam, respectively. Zhou et al. [18] proposed a pre-mining evaluation method of fault stability based on fault orientation, in-situ stress and pore fluid pressure, which can evaluate the risk of rock burst. Zhu et al. [19] found that stress mutation would induce fault slip; they proposed a break-tip blast to control fault stress and thereby reduce the risk of rock burst. The aforementioned research underscores that the intricate interplay of tectonic static stress, structural alterations in the roof, and fault-activated dynamic stress collectively contribute to the occurrence of rock burst. The specific disturbance mechanisms and the extent of their influence are intimately tied to the unique characteristics of fault preservation [20,21]. A penetrating fault is generally characterized by a throw that exceeds 5 to 20 m, with the maximum fault throw reaching hundreds of meters [22–25]. Furthermore, it is observed that the tectonic stress on the fault is typically positively correlated with the magnitude of the fault throw [14,26]. Therefore, fault protection coal pillars are strategically positioned within the working face to effectively isolate the influence of high tectonic stress, ensuring the safety of mining operations. A large amount of research focuses on elucidating the rock burst mechanism triggered by fault activation during mining near fault protection coal pillars. For instance, Cao et al. [27] and Bai et al. [28] posit that variations in displacement and stress within the overlying strata above the working face are the primary factors contributing to the activation of adjacent faults. Wang et al. [29] revealed that the loose space formed by the falling of overlying strata on the working face is necessary for fault activation and stress release. The unloading of horizontal and vertical principal stresses in the mining area serves as the primary factor influencing fault sliding. As the unloading of horizontal principal stresses intensifies, the possibility of fault sliding increases, exhibiting a trend that can be characterized as exponential [6,16,23,30,31]. Guo et al. [32] simplified the fault as a discontinuous boundary and studied the activation law of faults near the working face in response to decreasing stress levels within the activity of key strata. Kong et al. [17] verified this activation law through the variation of microseismic b-values on the fault plane. Fu et al. [33] and Kou et al. [34] revealed, through numerical simulations, that the stress evolution of surrounding rock during tunnel excavation through a penetrating fault comprises three distinct stages: reduction, rising, and stability. The research presented above indicates that mining disturbances outside the fault protection coal pillar can elicit the large-scale activation of a penetrating fault. Conversely, when

tunneling through the penetrating fault, the stress evolution within the surrounding rock in response to small-scale fault movements appears relatively simple. Unfortunately, this simplified stress evolution does not provide sufficient guidance for implementing effective rock burst prevention measures during the mining of the 501 working face in TB Coal Mine, as it mines through the penetrating fault.

Due to the irregular cutting of the working face [35] and the penetrating fault [36,37], triangular coal pillars are locally formed within the coal seam. Numerous scholars have delved into the influence of coal pillar width, height, and shape on its stress distribution characteristics. For instance, as the width of the coal pillar progressively increases, the length of the hanging roof above the working face gradually increases, subsequently stabilizing at a particular length. The stress evolution within the coal pillar exhibits three distinct stages: an initial low-stress phase, followed by a high-stress phase, and ultimately culminating in a stable stress state [38–44]. Zhu et al. [45], through their experiments, revealed that the rock burst risk of coal pillars initially intensifies and then gradually diminishes as the width-to-height ratio of the coal pillar increases. Notably, when the width-to-height ratio exceeds 3:1, the risk of coal pillar failure is minimized. Xue et al. [45] posit that there exists a notable disparity in the overlying strata structure on either side of an irregular coal pillar, resulting in an asymmetric stress distribution within the coal pillar. Furthermore, they observed a phenomenon of stress mutation where the shape of the coal pillar undergoes a transition [44].

The fault plane parameters exert additional influences on the stress within the coal pillar, particularly when the fault and triangular coal pillar combine to form a 'fault–coal pillar' structure [46], which can induce rock burst. For instance, Zhou et al. [47] experimentally demonstrated that the activation of fault planes with high and low roughness is stick-slip and stable slip, respectively, implying that the corresponding dynamic stress required for fault activation must differ. Feng et al. [48] investigated the influence of fault dip angle and azimuth angle on coal pillar stress through numerical simulation. They determined that when the fault dip angle and azimuth angle at a Hengda coal mine was 75° and 50°, respectively, the risk level associated with the rock burst of the triangular coal pillar reached its peak. A fault plane represents a discontinuous interface formed by loose rock masses [32]. The existence of faults exhibits a barrier effect on stress transmission [49]; currently, the study of the stress evolution in triangular coal pillars with varying widths, subject to the barrier effect of faults, remains unclear. This lack of understanding hinders the development of a theoretical foundation for targeted prevention measures aimed at mitigating rock burst in triangular coal pillars containing faults.

The stress concentration within the triangular coal pillar is primarily influenced by roof abutment stress [38]. Therefore, the prevention and control of rock burst in triangular coal pillars primarily focus on two aspects: (1) Reducing the length of the hanging roof and the excess stress on the triangular coal pillar by implementing roof cutting measures. The primary methods for this include roof blasting [50,51] and hydraulic fracturing [52]. (2) However, the implementation of roof cutting measures can compromise the support of the roadway. Furthermore, rock burst roadways require higher support strength to resist dynamic stress. Consequently, rock mass injections [36,53] are employed to control roof fragmentation in the triangular coal pillar area of the roadway, while additional cables [54–56] are used to reinforce the support and enhance the roadway's resistance to dynamic stress.

The current research focuses on elucidating the rock burst mechanism in the working face located outside the fault protection coal pillar, whereas the rock burst within the working face mining through the fault remains largely unexplored. While research examining the influence of coal pillar size, fault dip angle, and azimuth angle on the stress within triangular coal pillars adjacent to faults is relatively abundant, there is a notable lack of relevant research on the stress evolution of triangular coal pillars with varying widths under the barrier effect of faults. Rock burst cases [7,8] indicate that, although the microseismic triggering of the rock burst was located on the fault plane, the damage area

was primarily concentrated on the triangular coal pillars. The triangular coal pillar, being a rock burst risk area, is influenced by the superposition of tectonic stress, abutment stress, and fault barrier effects. As the working face mines through the penetrating fault, the width of the coal pillar varies, and under the barrier effect of the fault, the stress evolution within the triangular coal pillar exhibits increasingly complex characteristics.

This study focuses on the behavior of triangular coal pillars in the 501 working face of the TB mine during mining through the T6 penetrating fault, taking into account the fault barrier effect. Considering that surrounding rock stress contributes to the occurrence of rock bursts [57], the concept of fault barrier is introduced. Through theoretical analysis, the stress evolution under such conditions is investigated. Additionally, it reveals the specific rock burst mechanism in fault triangular coal pillars and enables the determination of rock burst risk levels for various pillar widths. Energy accumulates within the coal and rock mass, which serves as an indicator of the degree of damage caused by rock bursts [58,59]. Through numerical simulation, the accumulation pattern of energy within the fault triangular coal pillar is investigated, thereby identifying critical regions susceptible to rock burst damage. Based on these findings, targeted prevention and control measures are proposed to mitigate the risk of rock burst. This study aims to provide a useful reference for preventing rock bursts in similar fault triangular coal pillars.

## 2. Engineering Background

The depth of the 501 working face in the TB coal mine is approximately 500 m, with a dip length of 203 m and a strike length of 1103 m. It mines the M4-5 coal seam, with an average thickness and dip angle of 9 m and 18°, respectively. A 412 gob exists around the 501 working face, with a 40 m coal pillar separating the working face from the gob.

The 501 working face exposed 28 faults during mining, including 5 penetrating faults. Taking the T6 penetrating fault as an example, it had a dip angle of 75° and a drop of 2 m. The extension length of the penetrating T6 fault was significant, and its azimuth angle was 53°, bisecting the 510 working face in the dip direction, resulting in the formation of a triangular coal pillar with an included angle of 37°, as shown in Figure 1.

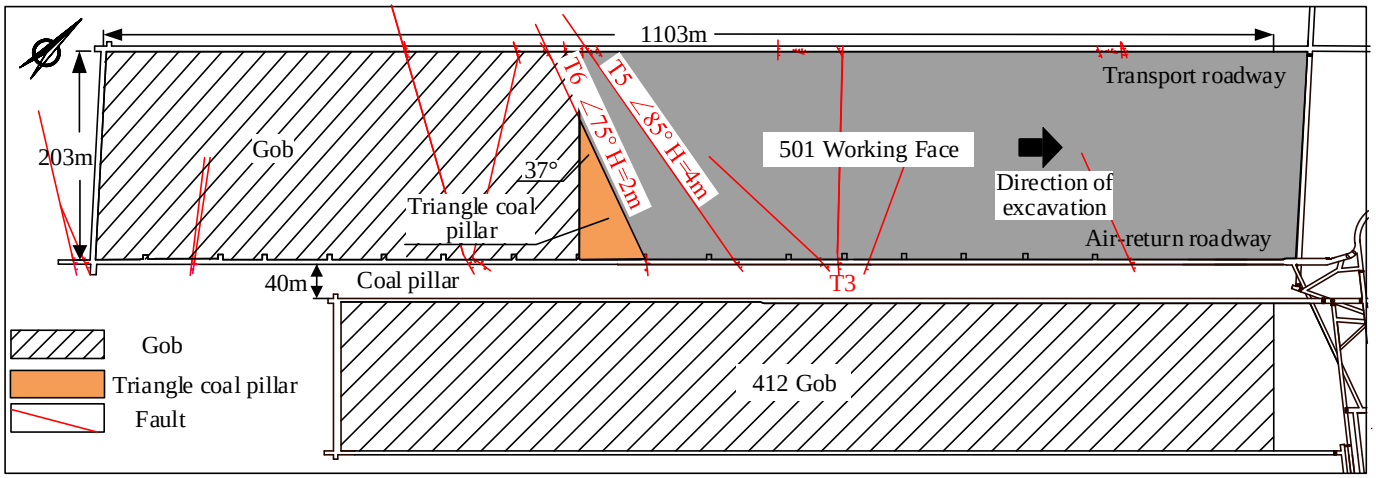



**Figure 1.** Triangular coal pillar position of 501 working face.

From 8 March 2021 to 7 April 2021, as the 501 working face was excavated 200 m away from the T6 penetrating fault, the energy and frequency of microseismic increased significantly, mainly concentrated in three areas: the 501 working face, the T6 and T5 penetrating faults, and the triangular coal pillar (as shown in Figure 2a). The analysis of the microseismic concentration area is presented in Figure 2b by quantifying the distribution of microseismic strike directions with step of 20 m.

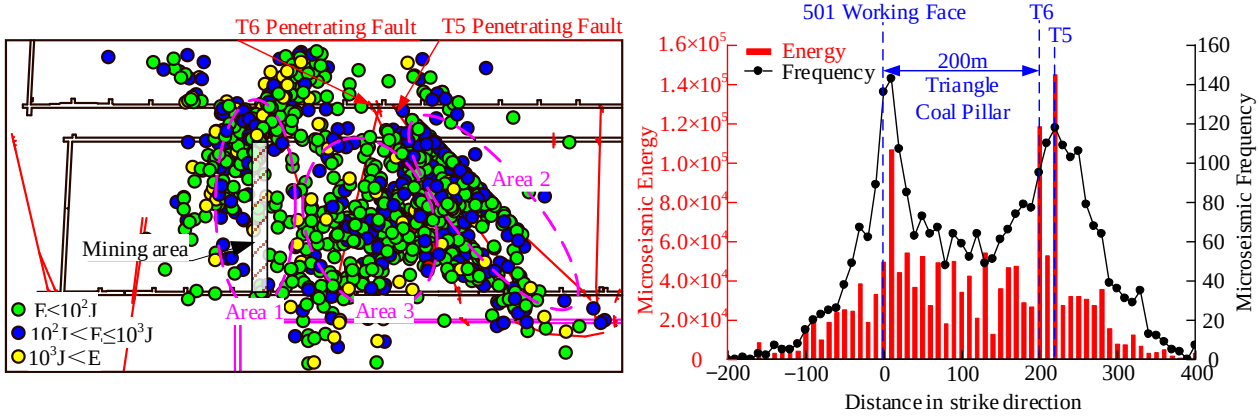



**Figure 2.** Microseismic distribution from 501 working face excavation to fault. (**a**) plane distribution of microseisms. (**b**) strike distribution of microseisms.

The support of the 501 working face roadway employs a combination of bolts and cables. The specifications for the bolts in the roof are φ22 mm × 2400 mm, with a row spacing of 1200 mm and a column spacing of 1000 mm. For the cables in the roof, the parameters are a diameter of 21.8 mm and a length of 7300 mm, with rows spaced at 1800 mm and columns spaced at 1000 m. Additionally, the parameters for the bolts in the walls of the roadway are φ22 mm × 2400 mm, with a row spacing of 800 mm and a column spacing of 1000 mm.

As the working face approached the fault, significant deformation was observed in both the roof and the walls of the roadway. Consequently, reinforcement measures were introduced by adding cables to the roof and walls of the roadway. Specifically, the roof reinforcement cables were upgraded to φ21.8 mm × 9300 mm, with two additional cables per row installed. Furthermore, the reinforcement for the walls of the roadway involved adding cables with a diameter of 21.8 mm and a length of 4300 mm, with one additional cable added every two rows.

Given the relatively intact condition of the on-site roof and walls of the roadway, rock mass injection measures were deemed unnecessary.

Area 1-501 working face: the microseismic energy and frequency were $1 \times 10^5$ J and 143, respectively, which are at a high level. Using the key stratum theory [60,61] to identify borehole 42-6, a sub key stratum of coarse sandstone with thickness of 37.18 m existed 30 m above the 501 working face, as shown in Figure 3. The breakage of the key stratum [62,63] caused the concentration of microseisms within 40 m around the working face.

Area 2-T6 and T5 penetrating fault: the fault was activated by abutment stress 200 m ahead of the working face [13,29]. Microseismic events were concentrated in 60 m around the T6 and T5 penetrating faults, and the maximum accumulated energy ranged from $1.11 \times 10^5$~$1.36 \times 10^5$.

In Area 3, the width of the triangular coal pillar was 200 m. The overall microseismic frequency and energy of the triangular coal pillar was 74.8% and 70.2% of the entire working face, respectively, indicating a high-level stress throughout the coal pillar. Additionally, the stress evolution in this area was intricate due to the varying width of the coal pillar.

| No | Lithology | Thicknesses | Depth |
|---|---|---|---|
| 1 | Loess soil | 12.21 | |
| 2 | Siltstone | 4.02 | 16.23 |
| 3 | Fine sandstone | 13.64 | 29.87 |
| | | | |
| 6 | Siltstone | 4.50 | 52.16 |
| 7 | Fine sandstone | 38.42 | 90.58 |
| 8 | Coarse sandstone | 10.49 | 101.07 |
| 9 | Siltstone | 34.76 | 135.83 |
| 10 | Mudstone | 2.00 | 137.83 |
| | | | |
| 12 | Coarse sandstone | 8.60 | 149.79 |
| 13 | Siltstone | 29.20 | 178.99 |
| 14 | Coarse sandstone | 3.20 | 182.19 |
| | | | |
| 24 | Coarse sandstone | 9.61 | 296.19 |
| 25 | Siltstone | 45.36 | 341.55 |
| 26 | Coarse sandstone | 1.95 | 343.50 |
| | | | |
| 29 | Coarse sandstone | 21.87 | 396.94 |
| 30 | Siltstone | 39.47 | 436.41 |
| 31 | Coarse sandstone | 37.18 | 473.59 |
| 32 | Siltstone | 10.20 | 483.79 |
| | | | |
| 35 | Mudstone | 6.89 | 493.29 |
| 36 | Siltstone | 8.04 | 501.33 |
| 37 | M4-5 coal seam | 9.48 | 510.81 |

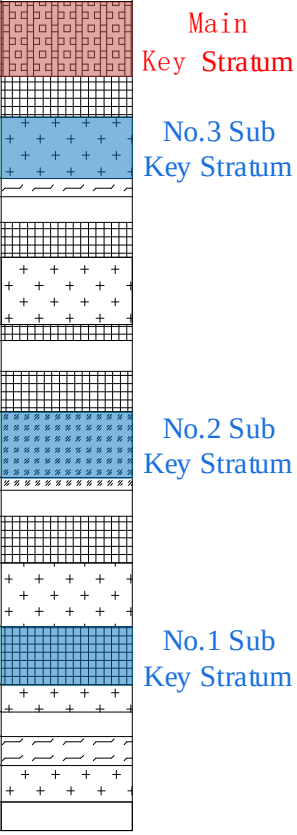



**Figure 3.** 42-6 Borehole.

## 3. Rock Burst Mechanism of Triangle Coal Pillar with Penetrating Fault

The stress level of triangular coal pillars is positively correlated with their rock burst risk [57]. The width variation of the triangular coal pillar during working face excavation directly affects its stress evolution and rock burst risk. The abutment stress exerted on the triangular coal pillar arises from the overlying strata above the goaf. Due to the barrier effect of the fault, the transmission of the abutment stress from the overlying strata is impeded, resulting in a concentration of abutment stress within the triangular coal pillar. Additionally, the tectonic stress within the fault structure further exacerbates the stress concentration within the triangular coal pillar, thereby increasing the level of rock burst risk in the fault-affected triangular coal pillar. Therefore, this section first establishes a theoretical model of the abutment stress of triangular coal pillars under fault barrier effects, analyzes the stress characteristics of triangular coal pillars under different fault barrier effects and coal pillar widths, and simultaneously considers the superposition effect of fault tectonic stress. It comprehensively identifies the risk level of triangular coal pillars with different widths and proposes the rock burst mechanism of triangular coal pillars.

### *Abutment Stress Characteristics of Triangle Coal Pillar with Penetrating Fault*

During the excavation of the 501 working face near the T6 penetrating fault, the key stratum sank and fractured under gravity. The hanging roof behind the workface was supported by the gob gangue, the triangular coal pillar, and the T6 fault plane [64].

Consequently, the mechanical model of triangle coal pillar abutment stress was established, as shown in Figure 4.

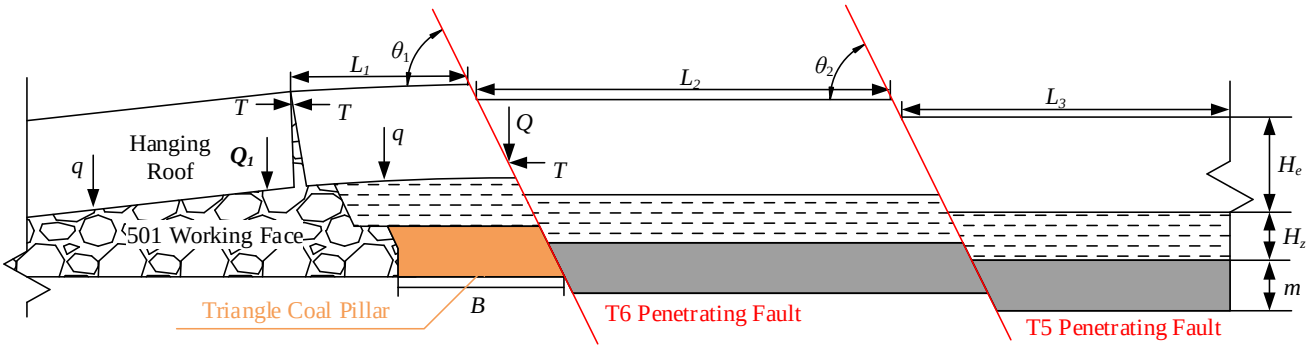



**Figure 4.** Mechanical model of triangle coal pillar abutment stress.

The stress transfer characteristics of the "voussoir beam" indicate that half of the hanging roof load was supported by the gangue, and the remaining half was supported by the triangular coal pillar and the fault plane [65].

The rock mass along the fault plane exhibits characteristics of weakness and fragmentation. This weak rock mass has the ability to impede the propagation of mining-induced stresses, leading to asymmetry in stress distribution on either side of the fault. When a fault transfers high stress from one plate to another, the fault plane will attenuate the transfer of mining stress to the other plate. The fault plane exhibits a barrier effect on stress transfer due to the inclusion of weakened and fractured rock [49,66]. Assuming a stress transfer coefficient $K$ for the fault plane, where the stress on the hanging wall of the fault is $\sigma_1$, and the stress transmitted to the footwall through the barrier effect of the fault plane is $\sigma_2$, the load transfer coefficient can be expressed as $K = \sigma_2/\sigma_1$. Here, $\sigma_1$ is a constant value and $\sigma_2$ ranges from 0 to $\sigma_1$, meaning that $K$ values range from 0 to 1. When $K$ = 1, it indicates that the fault has no barrier effect, and $\sigma_2 = \sigma_1$. When $K$ = 0, it indicates that the fault has a complete barrier effect, and at this time $\sigma_2 = 0$.

The load of roof In the gob area and the overlying triangular coal pillar transmitted across the fault to the hanging wall of the T6 fault can be expressed as:

$$Q = K\left(qL_1 + \frac{Q_c}{2}\right) = K\left(qL_1 + \frac{qL_1}{2}\right) = \frac{3KqL_1}{2} \quad (1)$$

In the formula, $Q$ represents the load transmitted from the sub key stratum to the hanging wall of T6 fault, kN/m; $Q_c$ denotes the load transmitted from the hanging roof to the working face, kN/m; $K$ stands for the load transfer coefficient of the fault plane, which is assigned a value of 0.8 based on the fragmentation observed on the T6 fault plane; $q$ is the load of the sub key stratum and is calculated as $q = \gamma h$, where $\gamma$ is the average bulk density of rock, 25 kN/m$^3$; $h$ represents the thickness of the rock stratum controlled by the sub key stratum, 75 m; and $L_1$ is the periodic weighting step of the 501 working face, taken as 20 m.

The load carried by the triangular coal pillar IIes the load that was not transmitted to the hanging wall of the T6 fault, and the gravity of the underlying rock of sub key stratum, as shown in Equation (2):

$$Q_B = \frac{3(1-k)qL_1}{2} + \gamma h_z\left(\frac{h_z \tan\theta}{2} + B\right) \quad (2)$$

In the formula, $Q_B$ is the load of the triangular coal pillar, kN/m; $H_z$ is the thickness of the underlying rock, which is 28 m; $\theta$ is the dip angle of the fault; and $B$ is the width of the triangular coal pillar, m.

The depth $h$ of the 501 working face is 500 m, then the abutment stress of the triangular coal pillar $q_B$ is determined by Equation (3):

$$q_B = \frac{\frac{3(1-k)qL_1}{2} + \gamma_z h_z \left(\frac{h_z \tan\theta}{2} + B\right)}{B} + \gamma h \tag{3}$$

The characteristics of abutment stress influenced by the width of the triangular coal pillar and the load transfer coefficient are analyzed in combination with Equation (3), as shown in Figure 5: (1) The abutment stress exhibits a negative correlation with the width of the coal pillar. When the width of the coal pillar is less than 50 m, the support stress increases exponentially. The abutment stress of 5 m triangular coal pillar reaches 17.2 Mpa, representing 29.3% increase compared to 50 m coal pillar. (2) The abutment stress exhibits a negative exponential correlation with the stress transfer coefficient. In particular, when the fault plane lacks barrier effect, indicating that the stress transfer coefficient is 1, the abutment stress reaches 12.1 Mpa. This value is 71.6% of that when the stress transfer coefficient is 0.1.

The uniaxial compressive strength of M4-5 coal in TB Coal Mine is 8.69 Mpa. Referring to the stress-based rock burst risk classification method [57], using 125%, 150%, and 175% (i.e., 10.86, 13.04, and 15.21 Mpa) of the uniaxial compressive strength of M4-5 coal as critical points, the weak rock burst, medium rock burst, and strong rock burst risk levels of the triangular coal pillar are classified, as shown in Figure 5a. When the width range of the triangular coal pillar is greater than 88 m, between 88 m and 11 m, and less than 11 m, it has weak rock burst risk, medium rock burst risk, and strong rock burst risk, respectively.

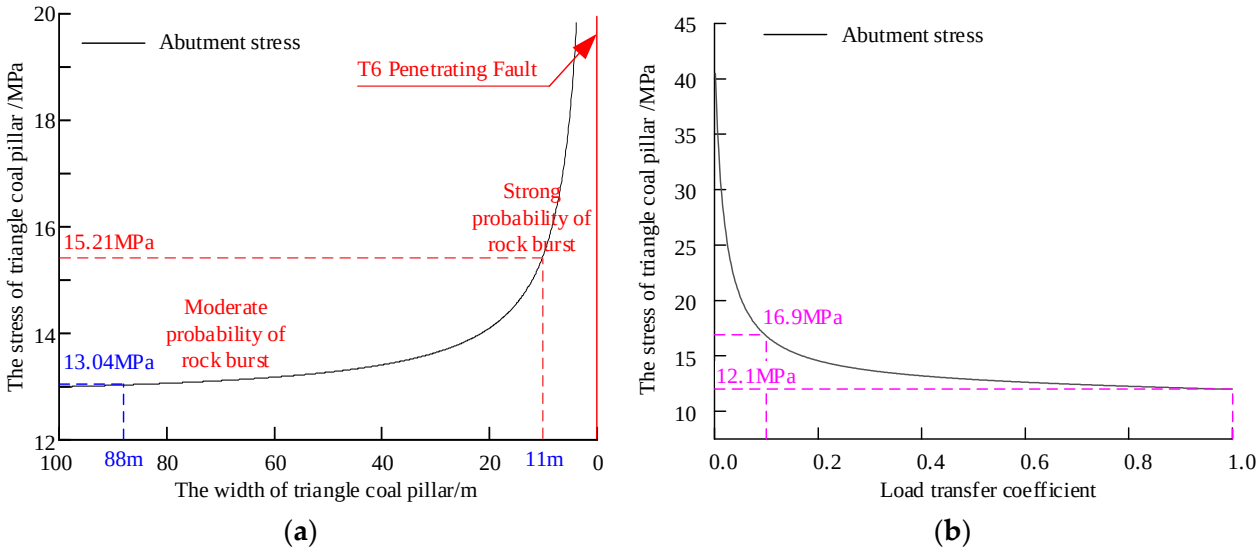



**Figure 5.** Abutment stress characteristics of triangle coal pillar. (**a**) influence of triangular coal pillar width. (**b**) influence of load transfer coefficient.

## 4. Tectonic Stress Characteristics of Triangle Coal Pillar with Penetrating Fault

The tectonic stress of a fault is determined by in-situ stress, fault dip angle, and fault length [67,68]. Simplify the fault along the dip profile into an elliptical fracture with a length of 2F, establish a complex coordinate system $z = x + iy$ based on the fault dip angle. $z$ represents the complex number of coordinates of any point in plane coordinate system; $x$ is the abscissa of the point, which is also the real part of the complex number $z$; and $y$ is the ordinate of the point, which is also the imaginary part of the complex number $y$. Through the conformal transformation of the complex function $\zeta = \xi + i\eta = \rho e^{i\varphi}$, $\zeta$ represents the complex number of coordinates of any point in the polar coordinate system; $\xi$ and $\eta$ have the same meanings as $x$ and $y$, respectively; $\rho$ represents the radius of any point in polar coordinates; and $\varphi$ represents the angle between any point in polar coordinates and the

horizontal plane. The infinite area outside the fracture is transformed into the unit circle of the coordinate system, as shown in Figure 6.

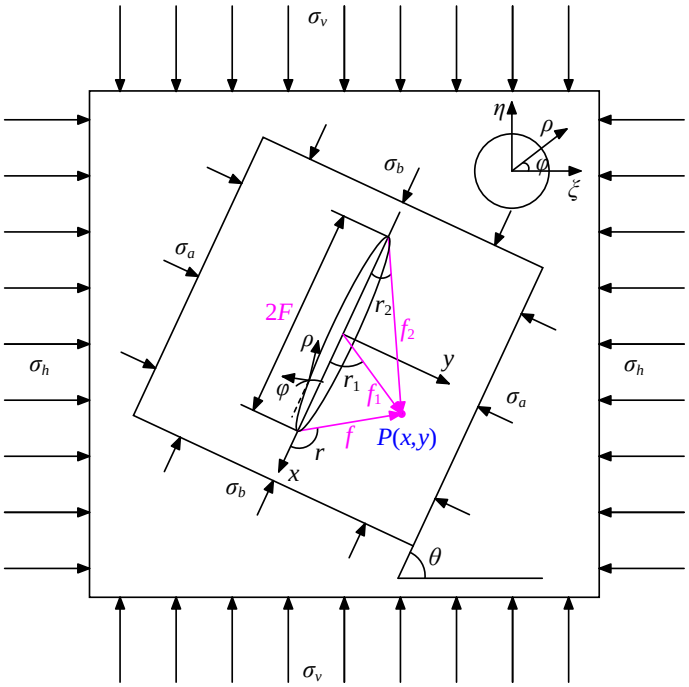



**Figure 6.** Tectonic stress increment mechanical model of faults.

According to the complex characteristics of stress components and boundary conditions, the tectonic stress increment at point $p$ around the fault is as follows:

$$\triangle\sigma_x = -\sigma_a(D - E - 1) \tag{4}$$

$$\triangle\sigma_y = -\sigma_a(1 - D - E) \tag{5}$$

$$\triangle\tau_{xy} = -\sigma_a F \tag{6}$$

In the formula, $D$, $E$, and $F$ are intermediate variables, represented as $D = (f_1/\sqrt{ff_1})\cos[r_1 - (r + r_2)/2]$; $E = \left[r^2 f_1/\sqrt{(ff_2)^3}\right]\sin r \sin[3(r + r_2)/2]$; $F = -\left[r^2 f_1/\sqrt{(ff_2)^3}\right]\sin r \cos[3(r + r_2)/2]$.

Where $f, f_1, f_2$ and $r, r_1, r_2$ are the distances and included angles from point $p$ to the right end, middle and left end of the fault, respectively; $\sigma_a$ can be converted from in-situ stress [69], $\sigma_a = \frac{\sigma_h + \sigma_v}{2} - \frac{\sigma_h - \sigma_v}{2}\cos 2\theta$, in which, $\sigma_h$ and $\sigma_v$ are horizontal and vertical in-situ stresses, respectively.

The distance between T6 and T5 penetrating faults is 50 m, meaning that the triangular coal pillar will be affected by the superposition of two tectonic stresses from both faults. The extension length of both T6 and T5 faults is 240 m, and the fault dip angles are 75° and 85° are substituted into the Formulas (4)~(6); the vertical tectonic stress increment in the triangular coal pillar is shown in Figure 7a. The tectonic stress around T6 and T5 faults is obviously asymmetric distribution, with the maximum tectonic stress increment reaching 24 MPa.

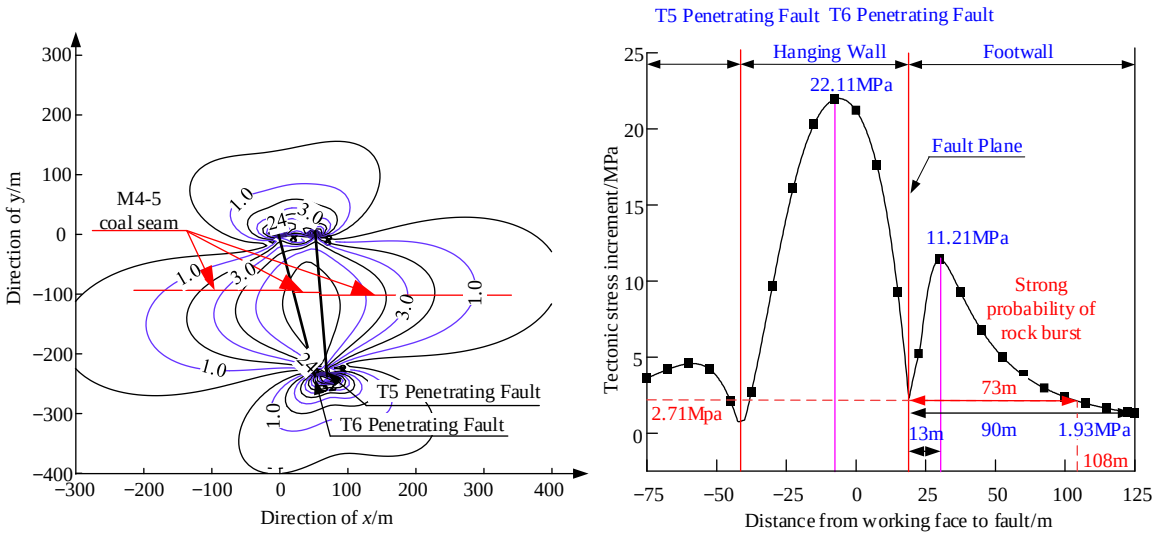



**Figure 7.** Tectonic stress increment of T6 and T5 penetrating faults. (**a**) distribution of tectonic stress. (**b**) characteristics of tectonic stress.

The tectonic stress monitoring line is established based on the spatial relationship between M4-5 coal seam and faults. The characteristics of tectonic stress in M4-5 coal seam are shown in Figure 7b. The triangular coal pillar located 90 m away from T6 fault is significantly influenced by tectonic stress, with the tectonic stress increment of 1.93 MPa. As the distance from the T6 fault decreases to 13 m, the tectonic stress peaks at 11.21 MPa. Furthermore, the middle section of the T5 and T6 faults is affected by the superposition of two faults, resulting in the maximum tectonic stress increment of 22.11 MPa.

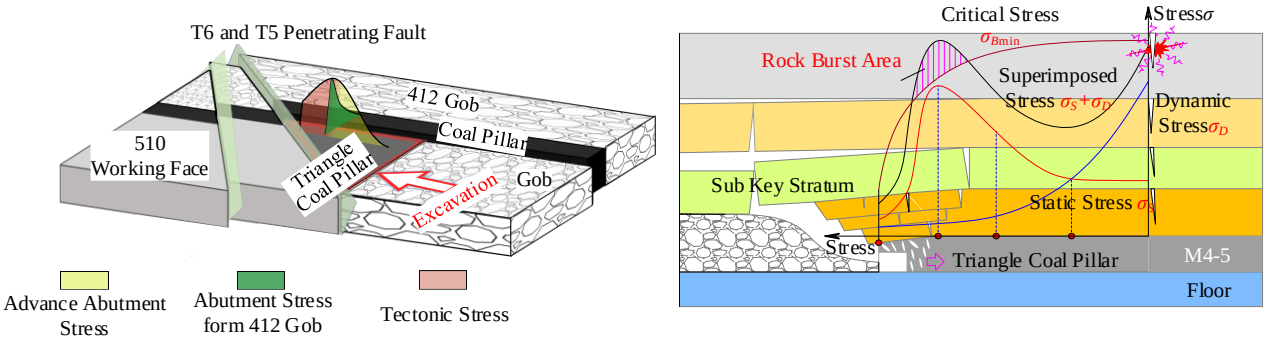
The M4-5 coal seam is buried at a depth of 500 m, with a vertical stress of 12.5 MPa. Therefore, the corresponding tectonic stress increment associated with a high rock burst risk is 2.70 MPa. Consequently, the coal pillar extending from 0 to 73 m away from the fault is categorized as a high rock burst risk area, as depicted in Figure 7b. Additionally, Figure 2b indicates that the T6 fault is active 200 m ahead of the working face. As a result, the coal pillar located within the range of 73 to 200 m from the fault is determined to be a medium rock burst risk area.

## 5. Rock Burst Mechanism of Triangle Coal Pillar

The triangular coal pillar situated between T6 penetrating faults, the 501 working face, and the 412 goaf is shown in Figure 8a. Affected by the stress barrier effect of fault, the tectonic stress, the abutment stress of the 412 gob, and the advance abutment stress are significantly concentrated in the triangular coal pillar. With the excavation of the 501 working face, the width of triangular coal pillar decreases, the abutment stress increases exponentially, and the peak value of tectonic stress moves closer to the working face, resulting in a sharp rise in static stress within the triangular coal pillar. The identification of the rock burst risk level of the triangular coal pillar, based on considering both the abutment stress and tectonic stress, follows the most unfavorable principle: the working face is situated at a distance ranging from 73 m to 200 m from the fault, classified as a moderate rock burst risk, and at a distance ranging from 0 m to 73 m from the fault (i.e., the width of the triangular coal pillar spans from 0 m to 73 m), classified as a high rock burst risk.

The high dynamic stress associated with fault activation is transferred to the triangular coal pillar, which is already under high static stress. Once the stress in the triangular coal pillar exceeds its bearing limit [57] ($\sigma_s + \sigma_d \geq \sigma_{B\min}$), a large amount of elastic energy is released nonlinearly [70], triggering rock burst. In the formula, $\sigma_s$ represents the static

stress within the coal-rock mass and $\sigma_d$ denotes the dynamic stress induced by mining tremors in coal and rock masses. The critical stress, denoted as $\sigma_{Bmin}$, is determined by introducing graded stress into rock burst prediction. When the coal–rock mass experiences a rock burst, the magnitude of $\sigma_{Bmin}$ is related to the mechanical properties of the coal–rock mass itself [71]. Therefore, the type of rock burst in the triangular coal pillar is characterized as "high static-high dynamic stress", as shown in Figure 8b.




(**a**) (**b**)

**Figure 8.** Rock burst mechanism of triangular coal pillar. (**a**) stress distribution of triangular coal pillar. (**b**) rock burst mechanism.

## 6. Stress and Energy Evolution of Triangular Coal Pillars

The previous section identified the rock burst risk levels in different areas of the triangular coal pillar. Considering the positive correlation between energy accumulation in the triangular coal pillars and the degree of rock burst damage, it is still imperative to study the energy accumulation patterns of these coal pillars using numerical simulations as the working face mines through faults. This will help determine the degree of rock burst damage and identify the appropriate stress relief measures.

### *Numerical Modelling of Triangular Coal Pillars*

FLAC3D (V5.0), as a continuous element numerical simulation software [72], can focus on exploring the stress evolution of triangular coal pillars as their width varies. Based on the geological conditions of the TB coal mine and the characteristics of the 501 working face, a numerical simulation model of a triangular coal pillar was established, as shown in Figure 9. The numerical model has dimensions of 1000 × 600 × 230 m in length, width, and height, respectively. It is internally divided into the 412 gob and the 501 working face, both of which have a strike and inclination length of 800 m and 200 m, respectively. The width of the coal pillar situated in the section between the two is 40 m.

In the numerical model, the thickness of the overlying strata above the M4-5 coal seam is approximately 200 m. Considering the depth of the 501 working face is 500 m, a vertical stress of 7.5 MPa was applied to the top of the model. According to in-situ stress tests at the TB coal mine, the horizontal stress is 1.5 times the vertical stress. Therefore, a horizontal stress of 11.25 MPa (calculated as 7.5 MPa × 1.5) should be applied to the model. The coal and rock masses within the 501 working face and adjacent goaf in the numerical model are modeled using the Mohr–Coulomb constitutive model [73,74]. The numerical model initially excavates the adjacent goaf areas, resulting in natural subsidence and damage to the overlying strata. This process aims to simulate and obtain the conventional lateral abutment stress characteristics of the adjacent goaf areas on the 501 working face.

The dip angles of the T6 and T5 penetrating faults in the numerical model are 75° and 85°, respectively, with drops of 2 m and 4 m, respectively. The distance between the faults is 50 m. Coal seam stress monitoring lines 1#, 2#, and 3# are arranged in the 501 working face and the triangular coal pillar along the transport roadway, the central part, and the air-return roadway. Additionally, a numerical model without faults was also established.

Both the numerical models, with and without faults, initially excavate the 412 working face. After stress equilibrium of models were reached, the 501 working face was excavated from the boundary in 10 m steps until it completely passed through T5 and T6 penetrating faults. At the same time, the evolution of stress and energy within the coal seam was monitored.

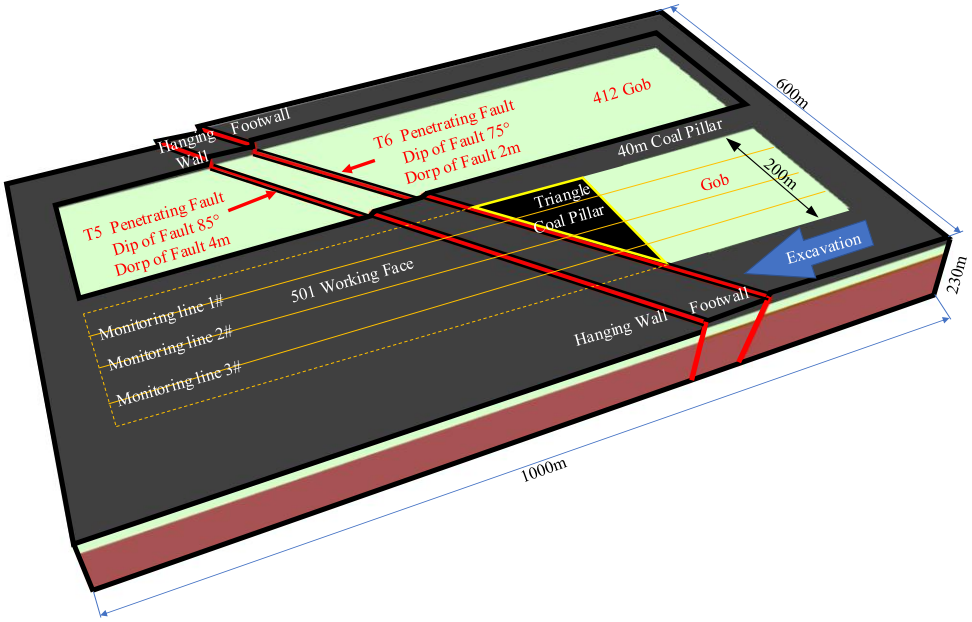



**Figure 9.** Numerical simulation model of triangle coal pillar.

The numerical simulation model employed the Mohr–Coulomb strength criterion. There was a notable difference in the mechanical parameters between the rock and rock mass. Based on the physical and mechanical parameters of the rock obtained from the 42-6 borehole, by utilizing the *RQD* index to convert the elastic modulus of the rock and the rock mass [75], the compressive strength of the rock mass could be calculated, as shown in Equation (7) and Table 1. The physical and mechanical parameters of the model are presented in Table 2.

$$\begin{cases} E_m / E_r = 10^{0.0186RQD-1.91} \\ \left(\frac{\sigma_{cm}}{\sigma_c}\right) = \left(\frac{E_m}{E_r}\right)^n \end{cases} \quad (7)$$

where $E_m$ and $E_r$ are elastic modulus of the rock and rock mass, respectively, GPa; $\sigma_{cm}$ and $\sigma_c$ are the uniaxial compressive strength of the rock and rock mass, respectively, MPa; and $n$ is the coefficient of weakening of the rock, which takes the value of 0.63; *RQD* index is determined by the 42-6 borehole.

**Table 1.** *RQD* conversion of rock and rock mass.

| Lithology | Rock | *RQD* | Rock Mass | |
|---|---|---|---|---|
| | Elastic Modulus Er/GPa | | Elastic Modulus Em/GPa | Shear Modulus/GPa |
| Coarse sandstone | 11.78 | 90 | 12.60 | 22.0 |
| Fine sandstone | 5.28 | 81 | 1.01 | 3.8 |
| Siltstone | 1.20 | 86 | 1.10 | 5.6 |
| Mudstone | 19.64 | 75 | 9.90 | 18.0 |
| M4-5 coal | 11.42 | 65 | 7.68 | 13.2 |

**Table 2.** Physical and mechanical parameters of model.

| Lithology | Density/(kg/m$^3$) | Bulk Modulus/GPa | Shear Modulus/GPa | Cohesive Force/MPa | Friction Angle/° |
|---|---|---|---|---|---|
| Coarse sandstone | 2700 | 30.0 | 22.0 | 130.0 | 38 |
| Mudstone | 2600 | 5.6 | 18.0 | 7.6 | 39 |
| Fine sandstone | 2700 | 19.4 | 3.8 | 12.8 | 35 |
| M4-5 coal | 1400 | 1.5 | 13.2 | 1.1 | 25 |
| Siltstone | 2500 | 13.1 | 5.6 | 3.0 | 33 |
| Fault plane | Cohesion force is 2.0 MPa, friction angle is 30° | | | | |

## 7. Stress Evolution of Triangular Coal Pillars

The stress at a distance of 150 m from the fault in the 501 working face is shown in Figure 10: (1) the abutment stress in the working face without fault first increased and then decreased, reaching a peak value of 25.3 MPa at 13 m ahead of the working face; (2) the monitoring line 3# first reached the T6 fault compared to monitoring lines 1# and 2#. Due to the barrier effect of the T6 fault, the abutment stress increased from 16.7 MPa to 22.8 MPa, an increase of 36.5%. The distance between the abutment stress peak and the working face was reduced to 8 m, and the peak stress reached 30.2 MPa. This indicates that there is a significant stress anomaly in the triangular coal pillar, which is consistent with the stress characteristics analyzed previously.

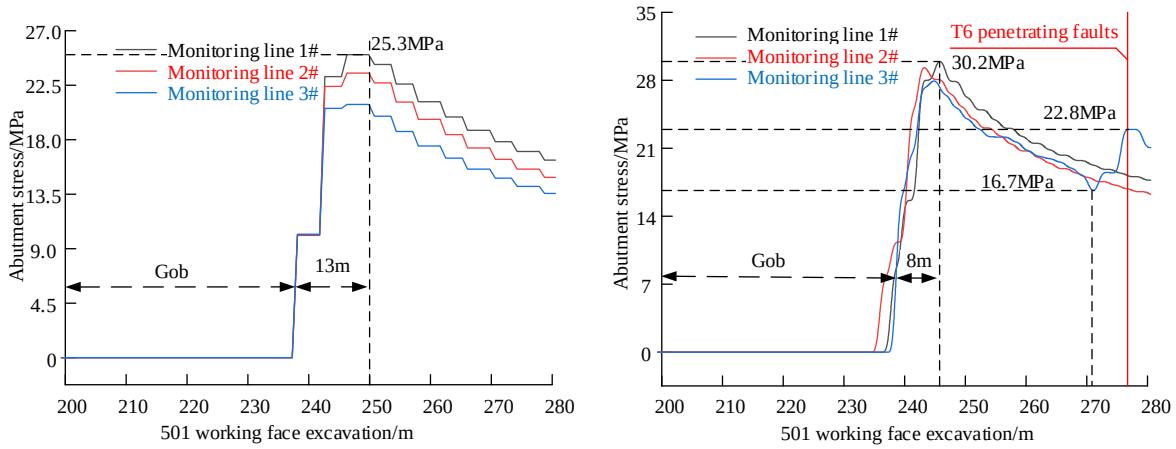



**Figure 10.** Stress characteristics of triangle coal pillar. (**a**) without fault. (**b**) under influence of fault.

The stress difference at 300 m, 150 m, and 50 m away from the fault was evident when comparing the 501 working face with and without the fault. Therefore, the stress nephograms for the above three stages are shown in Figure 11: (1) When the working face was excavated to 300 m away from the T6 fault, the triangular coal pillar area was primarily superimposed by advance abutment stress and the abutment stress from the 401 gob. Its peak stress was 20.0 MPa, which is basically consistent with model without fault. (2) When the working face was excavated to 150 m from the T6 fault, the triangular coal pillar area began to be affected by the tectonic stress. The stress increased by 0.1 MPa compared to the model without fault and increased by 16.3% compared with the initial excavation stage. (3) When the working face was excavated to 50 m from the T6 fault, the concentration of abutment and tectonic stress in the triangular coal pillar area was significant due to the fault barrier effect, and the peak stress reached 29.0 MPa, which was 17.4% higher than that of the non-fault model.

Stress concentration in coal is positively correlated with the risk of rock burst [76]. Under the barrier effect of the T6 fault, the abutment stress and tectonic stress in the triangular coal pillar began to rise at distance of 150 m from the fault, and the rock burst risk also rose. The peak stress increased significantly as the distance from the fault decreased, indicating that the narrower the width of the triangular coal pillar, the higher the rock burst risk.

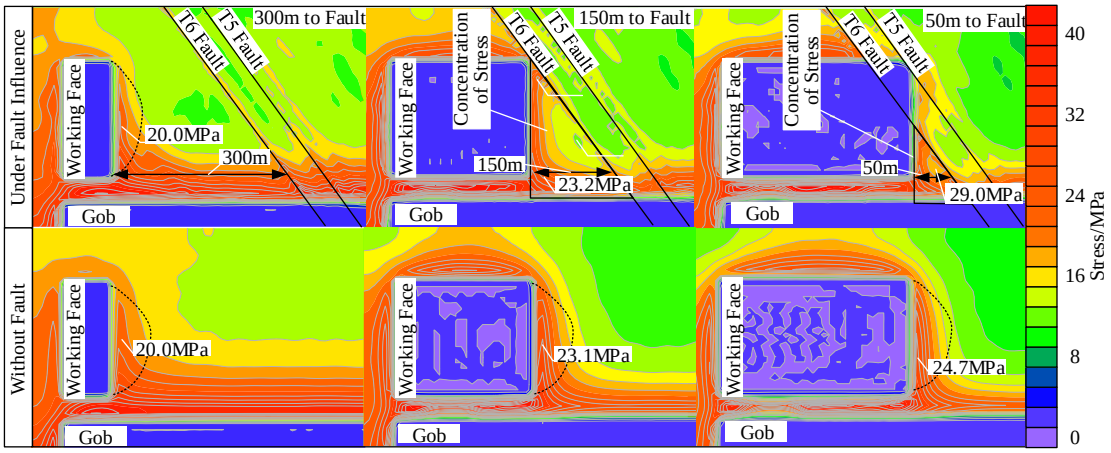



**Figure 11.** Stress evolution of triangle coal pillar.

## 8. Energy Evolution of Triangular Coal Pillars

Similar to the stress nephogram, the energy evolution of the 501 working face is shown in Figure 12: (1) When the working face was 300 m away from T6 fault, the energy density of the triangular coal pillar was 1.1 × $10^4$ J·$m^{-2}$, covering an area of 16 $m^2$, which is located in front of the working face. (2) When the working face was 150 m away from T6 fault, the energy density peak reached 1.20 × $10^4$ J·$m^{-2}$, representing a 9.1% increase. The area of energy concentration expanded to 50 $m^2$, a 212.5% increase, and the concentration area extended throughout the triangular coal pillar. (3) When the working face was 50 m away from T6 fault, the energy density of the triangular coal pillar increased by 81.8% compared with that 300 m away from the fault, and the maximum energy density reached 2.0 × $10^4$ J·$m^{-2}$. The energy concentration within the entire triangular coal pillar is significant.

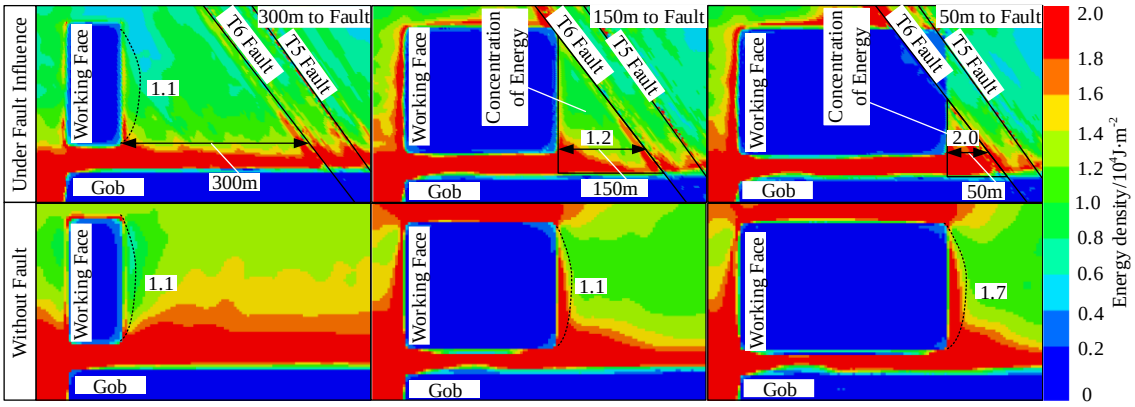



**Figure 12.** Energy evolution of triangle coal pillar.

The energy accumulation is positively correlated with the damage of rock burst [77]. When the working face was 150 m away from the fault, the energy density in the triangular coal pillar area began to rise significantly. As the width of the triangular coal pillar decreases,

the energy density within the coal pillar increased, and the concentration area expanded, indicating that the larger the rock burst damage area, the more severe the damage.

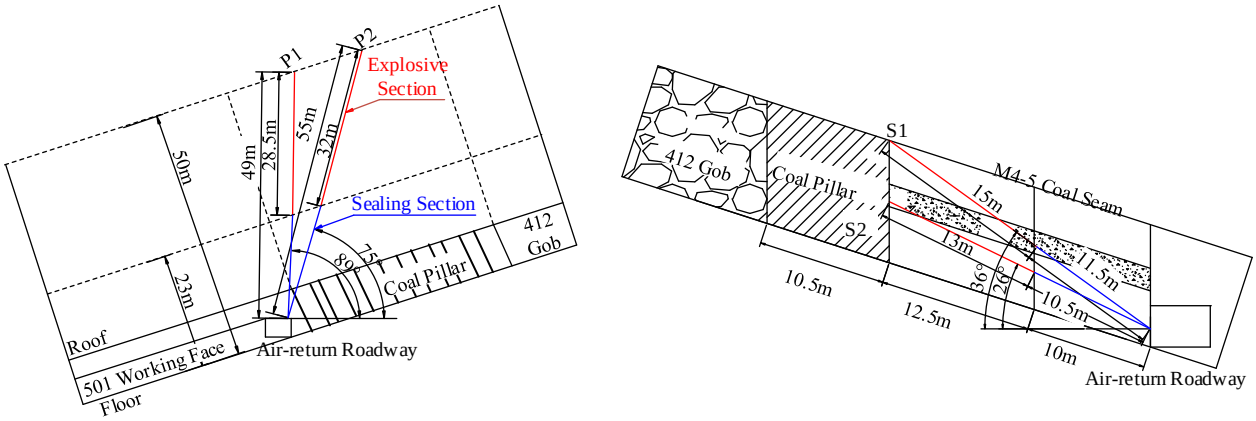
In summary, when the width of the triangular coal pillar reached 150 m, its energy accumulation rapidly increased, leading to an exacerbation of the rock burst damage. Therefore, stress relief measures should be implemented to enhance the effectiveness of stress relief. At a width of 50 m, the energy accumulation of the triangular coal pillar reached its peak. Under these conditions, stress relief measures should be optimized to achieve the highest level of stress release.

## 9. Engineering Case

*Measures of Stress Relief*

The stress evolution demonstrated that the triangular coal pillar stress began to rise significantly when its distance from the fault was less than 200 m, peaking at a distance of 73 m from the fault. Therefore, it is necessary to implement stress relief measures before the width of the triangular coal pillar affected by this stress increase reaches 200 m. These measures involve drilling large-diameter boreholes (150 mm diameter, 25 m depth) within the coal body, with a step spacing of 3 m. However, in the highly stressed region located within 0–73 m from the fault, the drilling step spacing should be reduced to 2 m to ensure adequate stress relief.

The energy evolution demonstrated that the triangular coal pillar energy began to rise at a distance of 150 m from the fault, peaking at a distance of 50 m from the fault. Therefore, different stress relief measures should be applied within the width range of 50–150 m and 0–50 m, respectively, in the triangular coal pillar to enhance the stress relief. The stress and energy within the triangular coal pillar is an abnormal concentration due to abutment stress from roof and tectonic stress from faults, both of which are under the influence of barrier effect. Therefore, the TB Coal Mine chose the air-return roadway, which is severely affected by the triangular coal pillar, for roof blasting in order to reduce abutment stress and for coal seam blasting to alleviate tectonic stress, as shown in Figure 13.




(**a**) (**b**)

**Figure 13.** Measures of stress relief. (**a**) stress relief blasting for roof. (**b**) stress relief blasting for coal seam.

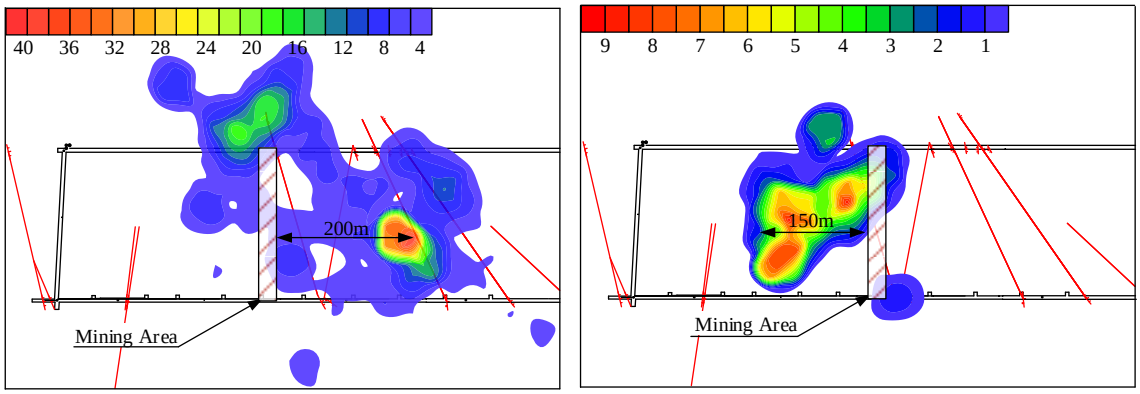
The maximum abutment stress generated by the sub key stratum under the influence of the barrier effect is 17.2 MPa, therefore blasting measures need to be taken. The blasting measures were implemented at a distance of 0~150 m from the fault in the air-return roadway, to enhance the stress relief of the triangular coal pillar. The spacing between blasting hole steps was 10 m. Each group included 2 blasting holes with a diameter of 75 mm, with elevation angles of 75° and 89°, and lengths of 49 m and 55 m, respectively. The blasting holes finally reached the middle of the sub key stratum. The length of explosives were 28.5 m and 32 m, respectively, and the amounts of the explosives were 50 kg and

56 kg, respectively. The application of roof blasting in high-stress areas of the working face may induce rock burst, while the restoration of surrounding rock stress can diminish the stress relief efficacy of blasting holes located far from the working face. Based on historical experience, it has been established that roof blasting measures should precede the mining face by approximately 200 m. Given that the average mining speed of the 501 working face is 4 m per day and the spacing between roof blasting holes is 10 m, the 501 working face implements roof blasting measures three times weekly

The triangular coal pillar exhibits significant stress concentration at a distance of 0~50 m from the fault, and it is necessary to carry out blasting measures on the coal seam. Implementing coal seam blasting holes at a distance of 50 m from the fault in air-return roadway maximizes stress relief on the triangular coal pillar. The step distance is 10 m. Each group comprises 2 blasting holes, with elevation angles of 36° and 26°, and lengths of 26.5 m and 23.5 m, respectively. The length of explosives are 15 m and 13 m, and the amounts of explosives were 36 kg and 31 kg, respectively. Similarly, given the average mining speed of 4 m per day of working and the step distance of 10 m between coal blasting holes in the 501 working face, coal blasting measures are implemented three times weekly.

## 10. Effectiveness of Stress Relief Measures

The rock burst energy [78] before and after the stress relief measures is shown in Figure 14: (1) before the stress relief measures, the rock burst energy was mainly concentrated near the fault, with a maximum index of 40; (2) after the stress relief measures, the rock burst energy was transferred to the gob, and the maximum index reached 9, which was 77.5% lower than that before the stress relief measures, and the range was significantly reduced. The stress relief measures transformed the microseismic from the fault activation to the roof caving behand working face, thus reducing the rock burst risk in air-return roadway.




(**a**) (**b**)

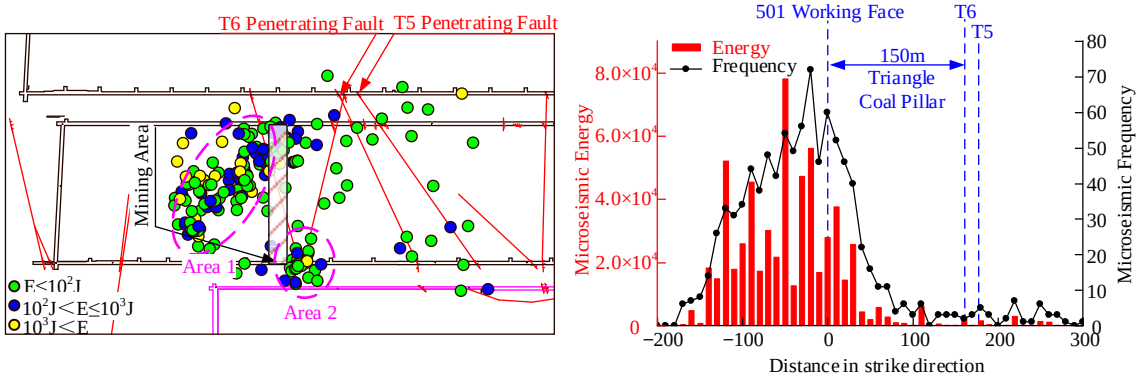
**Figure 14.** Rock burst energy nephogram. (**a**) before measures of stress relief. (**b**) after measures of stress relief.

Firstly, the microseismic monitoring area is gridded, and the microseismic background value is calculated based on the overall microseismic energy. Subsequently, the deviation between the microseismic energy of each grid and the background value is utilized to calculate the rock burst energy index.

$$E_{\varepsilon j} = \log_{10}\left(\frac{\sum\sqrt{E_i}}{A \cdot P}\right) \tag{8}$$

where $E_{\varepsilon j}$ is the rock burst energy index of the $j$-th region, which is the one divided by the longwall panel, $\log_{10}\sqrt{J}$; $E_i$ is the energy of the $i$-th microseismic, which belongs to the $j$-th statistical region, J; $A$ is the area of the $j$-th divided region, m$^2$; and $p$ is the statistical time, days.

The distribution characteristics of the microseismic at a distance of 150 m from the fault are shown in Figure 15. Compared with Figure 2b, the microseisms in front of the working face are significantly reduced and concentrated within 150 m behind working face. The maximum total energy of microseismic is $8.0 \times 10^4$ J, representing decrease of 70.0%. This indicates that the roof blasting measures effectively promote roof caving, while the coal blasting measures significantly reduce the stress concentration in the triangular coal pillar.




(**a**) (**b**)

**Figure 15.** Microseismic distribution from 501 working face after measures of stress relief. (**a**) plane distribution of microseisms. (**b**) strike distribution of microseisms.

## 11. Conclusions

This article theoretically analyzes the stress evolution law of triangular coal pillars, considering the influence of the fault barrier effect, overlying strata abutment stress, and fault tectonic stress. Numerical simulations were conducted to investigate the energy accumulation pattern within triangular coal pillars as the working face mining through the fault. Stress indicators were devised to categorize the rock burst risk regions and levels associated with triangular coal pillars, and tailored stress relief measures were proposed for various energy accumulation areas.

In contrast to conventional working faces outside fault protection coal pillars, the stress evolution and energy accumulation processes within triangular coal pillars in working faces mining through faults are more intricate. Thus, the stress and energy classification presented in this study offers a universal approach for identifying rock burst risks under complex stress conditions in triangular coal pillars. These research findings can provide valuable guidance for the prevention and control of rock bursts in similar mining cases involving penetrating fault triangular coal pillars.

The main conclusions from this research are as follows:

(1) The superimposed tectonic stress resulting from the T6 and T5 penetrating faults exhibited asymmetric distribution and had an influence range of about 90 m in the triangular coal pillar, reaching peak value of 11.21 MPa at a distance of 13 m from the fault plane.

(2) Affected by the barrier effect of penetrating faults, the abutment stress of the working face was concentrated in the triangular coal pillar, and the magnitude of the abutment stress was positively and negatively correlated with the fault plane barrier effect and the width of the triangular coal pillar, respectively.

(3) The barrier effect of the fault caused the stress and energy in the triangular coal pillar to increase as the width of the triangular coal pillar decreased. When the working face was 150 m away from the fault, energy and stress began to accumulate, and when the working face was 50 m away from the fault, energy and stress approached their peak.

(4) The constructed stress index indicates that triangular coal pillars possess moderate rock burst risks when their widths range from 73 to 200 m, and high rock burst risks when their widths are between 0 and 73 m. The analysis of the energy accumulation pattern within the triangular coal pillar reveals that the range of 50 to 150 m in width represents the most critical zone for implementing stress relief measures. Meanwhile, for the range of 0 to 50 m, specific measures should be undertaken to further enhance the effectiveness of stress relief.

(5) Roof blasting is employed to reduce abutment stress, and coal seam blasting is employed to reduce tectonic stress. After implementing the stress relief measures, the microseismic activity transformed from fault activation to roof caving, concentrated within range of 150 m behind the working face. The maximum total energy of microseismic was $8.0 \times 10^4$ J, a decrease of 70.0%, verifying the effectiveness of the stress relief measures.

**Author Contributions:** W.G. provided the complete research ideas and methods, provided the data used in this research, determined the title of this paper, and completed the compilation of the summary and conclusion. X.M. constructed a complete theoretical analysis and numerical simulation, and used the data for the verification of rock burst risk in the triangle coal pillar. W.G. determined the indicators used in the assessment of rock burst risk in the triangle coal pillar, and studied and confirmed the scientific and feasibility of the indicators. Y.W. and X.C. completed the verification of the full text, confirmed the correctness of the research results, provided innovative research ideas for this paper, and helped to complete the establishment of the rock burst prevention method. All authors have read and agreed to the published version of the manuscript.

**Funding:** This work was sponsored by the National Key Research and Development Program of China (2022YFC3004603); the Xinjiang Uygur Autonomous Region Key Research and Development Task Special Project (2022B01034); the National Natural Science Foundation of China (52274098); and the Jiangsu International Cooperation Project (BZ2023050).

**Data Availability Statement:** The raw data supporting the conclusions of this article will be made available by the authors on request.

**Acknowledgments:** Acknowledgment for the data support from TB Coal Mine and the engineering verification from Li Kang. A special acknowledgment should be shown to the anonymous reviewers for their constructive and valuable comments. Thank you to them for their guidance despite their busy schedule.

**Conflicts of Interest:** The authors declare no conflict of interest.

## References

1. Zhao, H.; Liao, Q.; Li, S.; Xiao, D.; Wang, G.; Guo, R.; Xue, Z.; Li, X. Early Paleozoic tectonic evolution and magmatism in the Eastern Tianshan, NW China: Evidence from geochronology and geochemistry of volcanic rocks. *Gondwana Res.* **2022**, *102*, 354–371. [CrossRef]
2. Mao, Q.; Ao, S.; Windley, B.F.; Zhang, Z.; Sang, M.; Tan, Z.; Wang, H.; Li, R.; Xiao, W.; Pan, Z. Middle–Late Triassic southward-younging granitoids: Tectonic transition from subduction to collision in the Eastern Tianshan–Beishan Orogen, NW China. *Geol. Soc. Am. Bull.* **2022**, *134*, 2206–2224. [CrossRef]
3. Wang, P.; Luan, H. Size effect analysis of remaining coal pillar on rock burst caused by fault. *Bull. Eng. Geol. Environ.* **2022**, *81*, 108. [CrossRef]
4. Danesh, N.; Nima, N.; Zhao, Y.; Teng, T.; Masoudian, M. Prediction of interactive effects of CBM production, faulting stress regime, and fault in coal reservoir: Numerical simulation. *J. Nat. Gas Sci. Eng.* **2022**, *99*, 104419. [CrossRef]
5. Zhang, L.; Shen, W.; Li, X.; Wang, Y.; Qin, Q.; Lu, X.; Xue, T. Abutment Pressure Distribution Law and Support Analysis of Super Large Mining Height Face. *Int. J. Environ. Res. Public Health.* **2023**, *20*, 227. [CrossRef]
6. Tai, L.; Li, C.; Gu, S.; Yu, X.; Xu, Z.; Sun, L. Research on dynamic response characteristics of normal fault footwall working face and rock burst prevention technology under the influence of the gob area. *Sci. Rep.* **2023**, *13*, 18676. [CrossRef]
7. Cai, W.; Dou, L.; Li, Z.; He, J.; He, H.; Ding, Y. Mechanical Initiation and Propagation Mechanism of a Thrust Fault: A Case Study of the Yima Section of the Xiashi-Yima Thrust (North Side of the Eastern Qinling Orogen, China). *Rock Mech. Rock Eng.* **2015**, *48*, 1927–1945. [CrossRef]
8. Wang, C.; Jiang, F.; Liu, J. Analysis on control action of geologic structure on rock burst and typical cases. *J. China Coal Soc.* **2012**, *37*, 263–268. (In Chinese)

9. Yang, Z.; Liu, C.; Zhu, H.; Xie, F.; Dou, L.; Chen, J. Mechanism of rock burst caused by fracture of key strata during irregular working face mining and its prevention methods. *Int. J. Min. Sci. Technol.* **2019**, *29*, 889–897. [CrossRef]
10. Zhu, S.; Ge, D.; Jiang, F.; Wang, C.; Li, D.; Shang, X.; Zhang, B.; Wang, Z. Rock Burst Mechanism under Coupling Action of Working Face Square and Regional Tectonic Stress. *Shock Vib.* **2021**, *2021*, 5538179. [CrossRef]
11. Wang, P.; Jiang, L.; Jiang, J.; Zheng, P.; Li, W. Strata Behaviors and Rock Burst-Inducing Mechanism under the Coupling Effect of a Hard, Thick Stratum and a Normal Fault. *Int. J. Geomech.* **2018**, *18*, 04017135. [CrossRef]
12. Li, Z.; Dou, L.; Cai, W.; Wang, G.; He, J.; Gong, S.; Ding, Y. Investigation and analysis of the rock burst mechanism induced within fault-pillars. *Int. J. Rock Mech. Min. Sci.* **2014**, *70*, 192–200. [CrossRef]
13. Xiao, Z.; Gu, S.; Zhang, Y.; Wang, H. An effective control method of rock burst induced by shear instability of fault structure under complicated geological conditions. *Bull. Eng. Geol. Environ.* **2023**, *82*, 105. [CrossRef]
14. Zhang, Q.; Zou, J.; Wang, J.; Jiao, Y.; Xu, H. Mechanism of coal bump induced by joint slipping under static and dynamic stresses in graben structural area. *Acta Geotech.* **2024**, *19*, 347–361. [CrossRef]
15. Jiang, F.; Yang, S.; Cheng, Y.; Zhang, X.; Mao, Z.; Xu, F. A study on microseismic monitoring of rock burst in coal mine. *Chin. J. Geophys. Chin. Ed.* **2006**, *5*, 1511–1516.
16. Cao, M.; Wang, T.; Li, K. A Numerical Analysis of Coal Burst Potential after the Release of the Fault-Slip Energy. *Rock Mech. Rock Eng.* **2023**, *56*, 3317–3337. [CrossRef]
17. Kong, P.; Liu, R.; Xing, L.; Li, Z.; Xu, C.; Zhang, Z. Study on the dynamic response and the hazard of rock burst under the influence of fault slip. *Front. Earth Sci.* **2023**, *10*, 1034332. [CrossRef]
18. Zhou, Q.; Liu, D.; Lin, X. Pre-evaluation of fault stability for underground mining based on geomechanical fault-slip analysis. *Geomat. Nat. Hazards Risk* **2022**, *13*, 400–413. [CrossRef]
19. Zhu, G.; Dou, L.; Liu, Y.; Su, Z.; Li, H.; Kong, Y.; Li, Z. Dynamic Behavior of Fault Slip Induced by Stress Waves. *Shock Vib.* **2016**, *2016*, 4386836. [CrossRef]
20. Li, Y.; Zhang, F.; Hu, L.; Zhuang, Z. Distinct element modelling of mining-induced instability of a heterogeneous fault. *Bull. Eng. Geol. Environ.* **2023**, *82*, 69. [CrossRef]
21. Fryer, B.; Giorgetti, C.; Passelegue, F.; Momeni, S.; Lecampion, B.; Violay, M. The Influence of Roughness on Experimental Fault Mechanical Behavior and Associated Microseismicity. *J. Geophys. Res. Solid Earth* **2022**, *127*, e2022JB025113. [CrossRef] [PubMed]
22. Sun, W.; Hao, J.; Dai, X.; Kong, L. Response mechanism characteristics of mining-induced fault activation. *Coal Geol. Explor.* **2024**, *52*, 12–20. (In Chinese)
23. Shan, R.; Liu, D.; Wang, H.; Tong, X.; Li, Z.; Zhao, Y. Study of the fracture instability and fault slip risk of overlying strata during mining near faults. *J. Geophys. Res. Solid Earth* **2023**, *82*, 94. [CrossRef]
24. Wang, H.; Tian, Z.; Wang, Q.; Liu, W.; Jiang, Y.; Shi, R. Investigation on the mutation effect induced by the coupled destabilization of fault and overburden rock strata during coal mining. *J. China Coal Soc.* **2023**, *48*, 2961–2975. (In Chinese)
25. Chen, S.; Zhang, X.; Shi, R.; Li, Z.; Feng, F.; Xia, Z.; Li, X. Formation process of thrust faults in coal measures and its influence on mining disaster. *J. China Coal Soc.* **2023**, *48*, 2995–3008. (In Chinese)
26. Cheng, X.; Qiao, W.; He, H.; Lusini, E.; Meng, X. Characteristics of regional geostress field and its impact on rock burst: A case study on the Binchang mining area, China. *Environ. Earth Sci.* **2023**, *82*, 612. [CrossRef]
27. Cao, M.; Yang, S.; Du, S.; Li, Y.; Wang, S. Study on fault-slip process and seismic mechanism under dynamic loading of hard roof fracture disturbance. *Eng. Fail. Anal.* **2024**, *163*, 108598. [CrossRef]
28. Bai, J.; Dou, L.; Li, J.; Zhou, K.; Cao, J.; Kan, J. Mechanism of Coal Burst Triggered by Mining-Induced Fault Slip Under High-Stress Conditions: A Case Study. *Front. Earth Sci.* **2022**, *10*, 884974. [CrossRef]
29. Wang, Q.; Wang, Y.; He, M.; Li, S.; Jiang, Z.; Jiang, B.; Xu, S.; Wei, H. Experimental study on the mechanism of pressure releasing control in deep coal mine roadways located in faulted zone. *Geomech. Geophys. Geo-Energy Geo-Resour.* **2022**, *8*, 50. [CrossRef]
30. Kong, P.; Wang, C.; Xing, L.; Liang, M.; He, J. Study on the fault slip rule and the rockburst mechanism induced by mining the panel through fault. *Geomech. Geophys. Geo-Energy Geo-Resour.* **2023**, *9*, 163. [CrossRef]
31. Kong, P.; Yuan, A.; Liu, Y.; Li, Z. Study on fault slip dynamic response and rock burst potential under the influence of different horizontal stresses. *Geomat. Nat. Hazards Risk* **2022**, *13*, 1321–1341. [CrossRef]
32. Guo, H.; Yu, W.; Wu, G.; Li, K.; Liao, Z. Mechanism of Stratum Instability and Dynamic Deformation under Discontinuous Boundary Conditions. *Appl. Sci.* **2024**, *14*, 1441. [CrossRef]
33. Fu, Q.; Yang, J.; Gao, Y.; Li, C.; Chang, X.; Wu, X. Mechanism and surrounding rock control of gob-side entry formation passing through normal fault: A case study. *Environ. Earth Sci.* **2023**, *82*, 603. [CrossRef]
34. Kou, H.; He, C.; Yang, W.; Wu, F.; Nie, J.; Xie, J.; Fu, J.; Xiao, L. Distribution Characteristics of In Situ Stress Field for a Deep-Buried Tunnel in the Fault Area. *Int. J. Geomech.* **2023**, *23*, 04023074. [CrossRef]
35. Chen, X.; Zhou, D.; Zhang, S.; Liang, X.; Dong, Y. Analysis and Prevention of Rock Burst Risk of Working Face under the Influence of Continuous Irregular Triangular Coal Pillar Stress Concentration Area. *ACS Omega* **2024**, *9*, 12927–12940. [CrossRef] [PubMed]
36. Xu, L.; Ma, Y.; Elmo, D.; Ding, S.; Zhu, H.; Liu, H.; Li, W.; Chen, W. Parameters and surrounding rock control of gob-side driving under double key stratum after roof cutting. *Sci. Rep.* **2024**, *14*, 5106. [CrossRef]
37. Wang, H.; Jiao, J.; Wu, Y.; Song, Y.; Xie, P.; Luo, S. Main factors that control roadway damage when a steeply dipping coal seam crosses a fault. *Geomat. Nat. Hazards Risk* **2024**, *15*, 2344798. [CrossRef]

38. Guo, J.; Ma, L.; Zong, D. Creep Damage Evolution Law and Stability Analysis of Remnant Coal Pillars in Longwall Goafs. *Int. J. Geomech.* **2024**, *24*, 04024116. [CrossRef]
39. Zang, C.; Jiang, B.; Wang, X.; Wang, H.; Zhou, J.; Chen, M.; Cong, Y. Study on damage law and width optimization design of coal pillar with the discrete element method. *Geomech. Eng.* **2024**, *37*, 555–563.
40. Du, F.; Li, Z.; Li, S.; Li, X.; Li, G.; Fan, X.; Ren, H.; Cao, Z. Breaking law of overburden rock and key mining technology for narrow coal pillar working face in isolated island. *Sci. Rep.* **2024**, *14*, 13045.
41. Zhou, H.; Huang, Q.; He, Y.; Wang, Q.; Wei, Y. A study on the mechanism and control technology of strong mine pressure in parallel coal pillar and hard roof mining. *Front. Earth Sci.* **2024**, *12*, 1407084. [CrossRef]
42. Sancer, J.; Petros, V.; Hudecek, V.; Zapletal, P. Strength and Deformation of Pillars during Mining in the Shaft Pillar. *Appl. Sci.* **2024**, *14*, 5003. [CrossRef]
43. Yu, W.; Fan, G.; Zhang, D.; Guo, W.; Zhang, W.; Zhang, S.; Fan, Z. Study on Characteristics of Front Abutment Pressure and Rational Stop-Mining Coal Pillar Width in Large Height Working Face. *Processes* **2024**, *12*, 1170. [CrossRef]
44. Huang, P.; Zhang, Q.; Xie, J.; Li, J.; Zhang, Q.; Li, M.; Simao, F. Multiscale study on coal pillar strength and rational size under variable width working face. *Front. Environ. Sci.* **2024**, *12*, 1338642. [CrossRef]
45. Zhu, Z.; Yao, Z.; Chen, K.; Lu, F.; Han, J.; Wang, L. Experimental study on the influence of width-height ratio on coal pillar type rock burst. *J. China Coal Soc.* **2024**, *49*, 1303–1317. (In Chinese)
46. Zhang, X.; Zhu, S.; Zhang, X.; Jiang, F.; Liu, J.; Chen, Y.; Wan, X.; Yang, T.; Zhu, C.; Li, J. Research on the mechanism of overall instability type rock burst of fault coal pillars in deep topsoil fully mechanized top coal caving mining area. *Chin. J. Rock Mech. Eng.* **2024**, *43*, 713–727. (In Chinese)
47. Zhuo, Y.; Liu, P.; Guo, Y.; Chen, H.; Zhang, L.; Chen, S. The different effects of polished and post-slip roughnesses on fault stability. *Tectonophysics* **2024**, *877*, 230281. [CrossRef]
48. Feng, X.; Zhao, X.; Ding, Z.; Hu, Q.; Wang, D.; Cao, Z. Numerical study on the influence of fault orientation on risk level of fault slip burst disasters in coal mines: A quantitative evaluation model. *Environ. Earth Sci.* **2024**, *83*, 94. [CrossRef]
49. Wang, X.; Guo, C.; Deng, C. Numerical modeling of fault barrier effects on three kinds of stresses: A case of footwall mining on the normal fault. *Prog. Geophys.* **2020**, *35*, 1605–1611. (In Chinese)
50. Xu, X.; Zhou, Y.; Yang, J.; Gao, Y.; Zhu, C.; Wang, Y.; Fu, Q. A new method of mining pressure control for roof cutting in advance working face. *Eng. Fail. Anal.* **2024**, *161*, 108302. [CrossRef]
51. Huang, W.; Zhao, T.; Zhang, C.; Liu, Y.; Sui, L.; Hou, T.; Jiang, D. Assessment of pillar stability and its control in a double roadway layout. *Energy Sci. Eng.* **2024**. [CrossRef]
52. Fang, X.; Xu, R.; Zhao, J. Research on instability of the triangular coal alongside the goaf in a fully mechanized top-coal caving work face. *J. China Univ. Min. Technol.* **2011**, *40*, 678–683. (In Chinese)
53. Cao, C.; Xie, Z.; Zhang, N.; Han, C.; Yan, G.; Mu, F.; Zhang, W. Differential roof cutting for roadway support in dual gob-side entry retention on a single working face—Multilevel continuous anchor-grouting control technology: A case study. *Eng. Fail. Anal.* **2024**, *163*, 108475. [CrossRef]
54. Skrzypkowski, K. A new design of support for burst-prone rock mass in underground ore mining. *E3S Web Conf. EDP Sci.* **2018**, *71*, 00006. [CrossRef]
55. Sun, X.; Wang, J.; Zhang, Y.; Zhao, W.; Guo, Z.; He, M.; Chen, F.; Miao, C. Stability control measures for roof cutting and NPR supporting of mining roadways in fault areas of kilometre-deep coal mine. *J. Mt. Sci.* **2023**, *20*, 3051–3065. [CrossRef]
56. Zhou, K.; Wu, J.; Kan, J.; Yang, K.; Zhao, X.; Li, Y. Bolting control of a coal roadway under multi-seam mining—A case study. *Arch. Min. Sci.* **2024**, *69*, 303–325. [CrossRef]
57. He, J.; Dou, L.; Gong, S.; Li, J.; Ma, Z. Rock burst assessment and prediction by dynamic and static stress analysis based on micro-seismic monitoring. *Int. J. Rock Mech. Min. Sci.* **2017**, *93*, 46–53. [CrossRef]
58. Jiang, F.; Liu, Y.; Zhai, M.; Guo, X.; Wen, J.; Liu, X.; Ma, X. Evaluation of rock burst hazard based on the classification of stress and surrounding rock. *Chin. J. Rock Mech. Eng.* **2017**, *36*, 1041–1052. (In Chinese)
59. Jiang, Y.; Pan, Y.; Jiang, F.; Dou, L.; Ju, Y. State of the art review on mechanism and prevention of coal bumps in China. *J. China Coal Soc.* **2014**, *39*, 205–213. (In Chinese)
60. He, J.; Li, W.; Fan, K.; Qiao, W.; Wang, Q.; Li, L. A method for predicting the water-flowing fractured zone height based on an improved key stratum theory. *Int. J. Min. Sci. Technol.* **2023**, *33*, 61–71. [CrossRef]
61. Miao, K.; Tu, S.; Wang, Y.; Li, J.; Zhao, H.; Guo, B. Utilization of broken rock in shallow gobs for mitigating mining-induced water inrush disaster risks and environmental damage: Experimental study and permeability model. *Sci. Total Environ.* **2023**, *903*, 166812. [CrossRef] [PubMed]
62. Zou, J.; Wu, K.; Zhang, X.; Zhu, J.; Zhou, Z.; Zheng, F.; Xie, H.; Jiao, Y. Effective evaluation of deep-hole blasting for controlling strong tremors induced by deep coal mining-A case study. *Int. J. Rock Mech. Min. Sci.* **2022**, *159*, 105211. [CrossRef]
63. Wang, H.; Wang, J.; Elmo, D.; He, M.; Ma, Z.; Gao, C. Ground response mechanism of entries and control methods induced by hard roof in longwall top coal caving panel. *Eng. Fail. Anal.* **2023**, *144*, 106940. [CrossRef]
64. Pan, C.; Xia, B.; Zuo, Y.; Yu, B.; Ou, C. Mechanism and control technology of strong ground pressure behaviour induced by high-position hard roofs in extra-thick coal seam mining. *Int. J. Min. Sci. Technol.* **2022**, *32*, 499–511. [CrossRef]
65. Wang, M.; Xu, Y.; Xu, Q.; Shan, C.; Li, Z.; Nan, H.; Li, Y.; Liu, H.; Chu, T. Stability control of overburden and coal pillars in the gob-side entry under dynamic pressure. *Int. J. Min. Sci. Technol.* **2023**, *170*, 105490. [CrossRef]

66. Jiao, Z.; Jiang, Y.; Zhao, Y.; Zhang, M.; Hu, H. Study of dynamic mechanical response characteristics of working face passing through reverse fault. *J. China Univ. Min. Technol.* **2019**, *48*, 54–63. (In Chinese)
67. Zhang, S.; Sun, K.; Li, K. Shale Reservoir Fracture Mechanism Under Impacts of Additional Stress Field and Leak-off. *J. Hunan Univ. Sci. Technol. Nat. Sci. Ed.* **2020**, *35*, 17–24.
68. Liu, Z.; Lyu, X.; Li, Y.; Zhang, H. Mechanism of faults acting on in-situ stress field direction. *Oil Gas Geol.* **2016**, *37*, 387–393.
69. Guo, W.; Cao, A.; Hu, Y.; Xue, C.; Liu, Y.; Lv, D. Stress distribution and rockburst characteristics of roadway group under the influence of fault and fold structures: A case study. *Geomat. Nat. Hazards Risk* **2022**, *13*, 736–761. [CrossRef]
70. Jiang, Q.; Feng, X.; Xiang, T.; Su, G. Rockburst characteristics and numerical simulation based on a new energy index: A case study of a tunnel at 2500 m depth. *Bull. Eng. Geol. Environ.* **2010**, *69*, 381–388. [CrossRef]
71. He, J.; Lin, M.; Liu, X.; Zhang, L.; Zhang, D.; Xiong, W.; Peng, Y. New method for introducing gradient stress into rock-burst prediction. *Chin. J. Geotech. Eng.* **2020**, *42*, 2098–2105. (In Chinese)
72. Zhu, Z.; Wu, Y.; Liang, Z. Mining-Induced Stress and Ground Pressure Behavior Characteristics in Mining a Thick Coal Seam With Hard Roofs. *Front. Earth Sci.* **2022**, *10*, 843191. [CrossRef]
73. Hu, J.; Wang, Y.; Ma, Z.; Ma, X.; Zhang, X.; Yu, G. Experimental and Numerical Analysis of Rock Burst Tendency and Crack Development Characteristics of Tianhu Granite. *Geofluids* **2021**, *2021*, 6681261. [CrossRef]
74. He, J.; Dou, L.; Mu, Z.; Cao, A.; Gong, S. Numerical simulation study on hard-thick roof inducing rock burst in coal mine. *J. Cent. South Univ.* **2016**, *23*, 2314–2320. [CrossRef]
75. Palmstrom, A. Measurements of and correlations between block size and rock quality designation (RQD). *Tunn. Undergr. Space Technol.* **2005**, *20*, 362–377. [CrossRef]
76. Cai, M. Principles of rock support in burst-prone ground. *Tunn. Undergr. Space Technol.* **2013**, *36*, 46–56. [CrossRef]
77. Gong, F.; Yan, J.; Li, X.; Luo, S. A peak-strength strain energy storage index for rock burst proneness of rock materials. *Int. J. Rock Mech. Min. Sci.* **2019**, *117*, 76–89. [CrossRef]
78. Wang, G.; Gong, S.; Li, Z.; Dou, L.; Cai, W.; Mao, Y. Evolution of Stress Concentration and Energy Release Before Rock Bursts: Two Case Studies from Xingan Coal mine, Hegang, China. *Rock Mech. Rock Eng.* **2016**, *49*, 3393–3401. [CrossRef]


**Disclaimer/Publisher's Note:** The statements, opinions and data contained in all publications are solely those of the individual author(s) and contributor(s) and not of MDPI and/or the editor(s). MDPI and/or the editor(s) disclaim responsibility for any injury to people or property resulting from any ideas, methods, instructions or products referred to in the content.